

Three-dimensional characterization of non-gaussian water diffusion in humans using diffusion kurtosis imaging

Hanzhang Lu,^{1*} Jens H. Jensen,¹ Anita Ramani¹ and Joseph A. Helpert^{1,2,3}

¹Department of Radiology, Center of Biomedical Imaging, New York University School of Medicine, New York, NY 10016, USA

²Department of Physiology and Neuroscience, New York University School of Medicine, New York, NY 10016, USA

³Department of Psychiatry, New York University School of Medicine, New York, NY 10016, USA

Received 12 September 2005; Revised 4 November 2005; Accepted 11 December 2005

ABSTRACT: Conventional diffusion tensor imaging (DTI) measures water diffusion parameters based on the assumption that the spin displacement distribution is a Gaussian function. However, water movement in biological tissue is often non-Gaussian and this non-Gaussian behavior may contain useful information related to tissue structure and pathophysiology. Here we propose an approach to directly measure the non-Gaussian property of water diffusion, characterized by a four-dimensional matrix referred to as the diffusion kurtosis tensor. This approach does not require the complete measurement of the displacement distribution function and, therefore, is more time efficient compared with the *q*-space imaging technique. A theoretical framework of the DK calculation is established, and experimental results are presented for humans obtained within a clinically feasible time of about 10 min. The resulting kurtosis maps are shown to be robust and reproducible. Directionally-averaged apparent kurtosis coefficients (AKC, a unitless parameter) are 0.74 ± 0.03 , 1.09 ± 0.01 and 0.84 ± 0.02 for gray matter, white matter and thalamus, respectively. The three-dimensional kurtosis angular plots show tissue-specific geometry for different brain regions and demonstrate the potential of identifying multiple fiber structures in a single voxel. Diffusion kurtosis imaging is a useful method to study non-Gaussian diffusion behavior and can provide complementary information to that of DTI. Copyright © 2006 John Wiley & Sons, Ltd.

KEYWORDS: diffusion; kurtosis; DKI; DTI; non-Gaussian

INTRODUCTION

Diffusion-weighted imaging (DWI) and diffusion tensor imaging (DTI) have been widely used to study water diffusion properties in the brain, particularly for white matter fibers (1–8). While these techniques can characterize the average diffusion distance of water molecules in three-dimensional space, they are not able to provide more specific information about the micro-environment that the water spins are located in. For example, the apparent diffusion coefficient (ADC) and diffusion tensor (DT) can indicate that the water diffusion distance is small, but they cannot differentiate whether the small diffusion distance is due to a more viscous environment or the presence of more barriers, such as cell membranes. This is because DTI theory assumes a perfect Gaussian distribution for the water molecule movement (9), but water in biological structures often shows non-Gaussian

diffusion behavior. As a result, the MR signal decay in tissue is not a simple monoexponential function of the *b*-value (10–17). Clearly, water diffusion has the potential of providing information beyond that given by the diffusion tensor.

The three-dimensional (3D) properties of water diffusion can be completely described using a displacement probability density function (18). Several MRI techniques have been devised to measure such 3D functions (11,19–21) generally referred to as *q*-space imaging. While these studies have demonstrated the great potential of *q*-space imaging, which can provide significantly more detailed information regarding water diffusion, they have been mostly applied to animal applications and *ex vivo* studies (11,18,19,22). The main reason for this is that *q*-space imaging methods pose a great demand on the imaging hardware and acquisition time, which are challenging for many clinical applications (18).

On the other hand, it has been increasingly demonstrated that the MR signal is not a simple monoexponential function of *b* value. Many investigators have observed a nonlinear decay of $\ln(S)$ when more than two *b* values are acquired (12–15,23–25). To account for such observations, biexponential fitting has been proposed, from which the two components can hypothetically reflect two separate biophysical compartments (12,23).

*Correspondence to: H. Lu, 650 First Avenue, 600A, Department of Radiology, New York University, New York, NY 10016, USA.

E-mail: h.lu@med.nyu.edu

Contract/grant sponsors: Werner Dannheisser Trust; Institute for the study of Aging.

Abbreviations used: FOV, field-of-view; FWHM, full-width-half-maximum; NEX, number of excitations; SENSE, sensitivity encoding; SPM, statistical parametric mapping; SNR, signal-to-noise ratio; *TE*, echo time; *TR*, repetition time.

However, with a typical spatial resolution of several millimeters, a brain voxel is likely to contain multiple tissue types, such as gray matter, white matter, cerebrospinal fluid (CSF) and blood. More importantly, it should be pointed out that nonlinear behavior of $\ln(S)$ is not an automatic indication of multi-compartment voxel composition. Even a single-compartment voxel with diffusion barriers can have a nonlinear signal decay (26).

Recently, we have developed an MR method (27) to directly investigate the non-Gaussian properties of water diffusion by measuring the kurtosis (28) of the displacement distribution function. This diffusion kurtosis represents the extent to which the diffusion pattern of the water molecules deviates from a perfect Gaussian curve. It differs from the biexponential model in that our method does not make assumptions on the number of biophysical compartments or even the existence of multiple compartments. In our previous paper (27), a general theory was proposed and it was also shown experimentally that apparent kurtosis coefficients (AKC) for a given direction can be robustly determined using the proposed method.

In this paper, we extend the diffusion kurtosis theory for quantitative measurement of the diffusion kurtosis (DK) tensor. Similar to the diffusion tensor, the 3D kurtosis properties of water diffusion can be completely described by a tensor, which is a fully symmetric $3 \times 3 \times 3 \times 3$ matrix with 15 independent elements. We demonstrate that the DK tensor can be quantified in humans within a clinically feasible time (~ 10 min) on a clinical scanner. The acquired data set also yield the conventional diffusion tensor. Furthermore, to facilitate the representation of the 3D kurtosis properties, a decomposition method, the spherical harmonics expansion, is applied to reduce the high-order matrix to several simple indices. It is also shown that diffusion kurtosis imaging (DKI) has the potential to provide information distinct from that given by the conventional diffusion tensor.

THEORY

Calculation of DK tensor

As described in our previous paper (27), the AKC for a single direction can be determined by acquiring data at three or more b values (including $b = 0$) and fitting to the equation:

$$\ln[S(b)] = \ln[S(0)] - b \cdot D_{\text{app}} + \frac{1}{6} b^2 \cdot D_{\text{app}}^2 \cdot K_{\text{app}} \quad (1)$$

where D_{app} is the apparent diffusion coefficient for the given direction, K_{app} is the apparent kurtosis coefficient and is a dimensionless parameter. Equation (1) is similar to the conventional ADC calculation except for an

additional quadratic term. Upon fitting the experimental data, both AKC and ADC can be obtained.

The non-Gaussian behavior of water diffusion in the three-dimensional space can be completely characterized by a kurtosis tensor, W_{ijkl} , which is a $3 \times 3 \times 3 \times 3$ matrix with 81 elements, where i, j, k and l are indices of the directions in the physical space, and can take on values of 1, 2 or 3. Owing to the full symmetry of the tensor, only 15 elements are independent: $W_{1111}, W_{2222}, W_{3333}, W_{1112}, W_{1113}, W_{1222}, W_{2223}, W_{1333}, W_{2333}, W_{1122}, W_{1133}, W_{2233}, W_{1123}, W_{1233}, W_{1233}$.

The DK Tensor (W_{ijkl}) is related to the AKC (K_{app}) in an individual direction by:

$$K_{\text{app}} = \frac{M_D^2}{D_{\text{app}}^2} \cdot \sum_{i=1}^3 \sum_{j=1}^3 \sum_{k=1}^3 \sum_{l=1}^3 n_i n_j n_k n_l W_{ijkl} \quad (2)$$

where

$$M_D = \frac{1}{3} \sum_{i=1}^3 D_{ii}$$

is the mean diffusivity and is independent of the direction, and n_i is the component of the direction unit vector. Equation (2) is a linear equation with 15 unknown parameters (see the Appendix). Therefore, by applying the gradients in 15 or more non-collinear, non-coplanar directions, one can solve equation (2) and obtain the complete DK tensor.

Spherical harmonics expansion of kurtosis angular plot

The 3D kurtosis property of water diffusion can be represented by an angular plot, $K_{\text{app}}(\theta, \phi)$ (see Results section for more details), where θ is the polar angle and ϕ is the azimuthal angle. Each point on the surface indicates the AKC for a particular direction as calculated from equation (2). However, it is difficult to quantify and compare 3D structures. Therefore, it is desirable to extract specific indices from the 3D surface plots so that the kurtosis in different patients or different brain regions can be easily compared. Thus we use the spherical harmonics expansion approach to decompose $K_{\text{app}}(\theta, \phi)$ into different components. The detailed theory of this method can be found elsewhere (29). In general, any angular function can be decomposed into an infinite number of spherical harmonics. However, owing to the limited number of degrees of freedom for the DK tensor, only the zero to fourth order harmonics of $K_{\text{app}}(\theta, \phi)$ contain independent information. Moreover, the geometric symmetry of the 3D structure dictates that the odd order harmonics ($l = 1$ and $l = 3$) vanish. Therefore, the expansion of $K_{\text{app}}(\theta, \phi)$ contains only 0th order, 2nd order and 4th order components, with each component order having $2l + 1$ coefficients. To further reduce the number of parameters representing $K_{\text{app}}(\theta, \phi)$, the coefficients for

the same order are combined and a rotationally invariant power index, C_l , is defined as:

$$C_l = \frac{1}{\sqrt{4\pi}} \sqrt{\left(\sum_{m=-l}^l A_{lm}^* \cdot A_{lm} \right)} \quad (3)$$

where A_{lm} are the coefficients with order l . The harmonic power indices can be used to describe the general features of the 3D kurtosis angular plot independent of the sample orientation in the magnet. Similar to the trace and fractional anisotropy (FA) of the diffusion tensor, each can be used as a new MR contrast parameter. Note that $1/\sqrt{4\pi}$ is the normalization factor. It is important to point out that the 0th power, C_0 , equals the mean kurtosis averaged over all possible angular directions.

METHODS

MRI experiment

The experiments were conducted on a 3 T MR system (Trio, Siemens Medical Solutions, Erlangen, Germany) using a body coil for transmission and an eight-element phase array coil for reception. The protocol was approved by the Institutional Review Board of the New York University School of Medicine. Four healthy volunteers (aged 28–44, two men and two women) gave informed written consent before participating in the study.

The DKI experiments were performed using a twice-refocused-spin-echo (TRSE) diffusion sequence (30). The TRSE sequence has been shown to significantly reduce the eddy-current-related distortions in the diffusion weighted images (30). We used a total of 30 gradient directions, which are homogeneously distributed on the unit sphere (31,32). For each direction, six b values ($b = 0, 500, 1000, 1500, 2000$ and 2500 s/mm^2) were used. Other imaging parameters were: $TR = 2000 \text{ ms}$, $TE = 108 \text{ ms}$, $FOV = 320 \times 320 \text{ mm}^2$, matrix = 128×128 , SENSE factor 2, NEX = 2, 13 axial slices, slice thickness = 2.5 mm , voxel size $2.5 \times 2.5 \times 2.5 \text{ mm}^3$. The total duration was 10 min and 20 s. In one subject, the protocol was repeated three times to test the reproducibility.

A phantom experiment using a fresh, intact asparagus was also performed with the following parameters: $TR = 2000 \text{ ms}$, $TE = 103 \text{ ms}$, $FOV = 100 \times 100 \text{ mm}^2$, matrix 64×64 , NEX = 32, one slice, slice thickness = 10 mm , $b = 0, 400, 800, 1200, 1600$ and 2000 s/mm^2 . The asparagus contains parallel fibers and can simulate the situation in white matter.

Data processing

The data were processed using in-house MATLAB (Mathworks, Natick, MA, USA) scripts. The preprocess-

ing included 3D motion correction using SPM (University College London, UK) and spatial smoothing using a Gaussian filter (FWHM = 3 mm). The smoothing procedure was found to be useful in improving the reliability of the estimation. The data at each gradient direction were fitted to equation (1) on a voxel-by-voxel basis to obtain the maps of ADC and AKC using Levenberg–Marquardt nonlinear fitting algorithm (33). To account for the possible effects of noise in the modulus data fitting, a noise term was also included in the nonlinear model (27). The noise amplitude, η , was estimated from a non-brain area (a 10×10 matrix in the upper left corner for 13 slices and six b values) containing 7800 voxels. The noise was considered as Rician noise, and therefore can be estimated by mean (all noise points) $\times 1.25/\sqrt{(\text{number of averages})}$ as confirmed by numerical simulations. The DT was calculated using ADC [obtained using equation (1)] in the 30 directions, from which the mean diffusivity, M_D , can be obtained. The DT was also used to calculate back the diffusion coefficient, ADC, in each of the 30 experimental gradient directions and these tensor-derived diffusion coefficients, instead of the ADC directly obtained from equation (1), were used to compute the DK tensor. The DK tensor, W , was computed by solving the linear equation group specified in equation (3) (15 unknowns, 30 equations). The total amount of time needed to process one complete data set (voxel-by-voxel basis for a $128 \times 128 \times 13$ matrix) was approximately 1 hour and 20 minutes on a standard desktop PC (CPU speed 3.2 GHz).

Various aspects regarding the reliability of the kurtosis estimation were assessed. (1) the reproducibility of results was evaluated by calculating the standard deviation of three repetitions; (2) the effects of the noise term were investigated by comparing the results with and without inclusion of noise in the model; (3) numerical simulations were performed to evaluate whether noise in the data can cause bias in the fitting results, and possible requirements for the SNR were studied; (4) the effects of spatial filtering were studied by comparing results before and after the filter application; and (5) the effects of possible motion in the data were studied by simulating random motion in one data set.

It is well established that the DT can be visually represented by an angular plot [e.g. Fig. 4(b) and (c)], on which each point indicates the ADC measured in that particular direction (15,17,21,34,35). Similar representation can be applied for the 3D kurtosis visualization by using equation (2) to calculate the AKC in many directions and plotting them on a 3D surface plot [e.g. Fig. 4(d) and (e)]. The angular plots shown in this study were from regions-of-interest (ROI) located in corpus callosum (CC) (seven voxels), gray matter (four voxels), occipital white matter (eight voxels), and a synthetic ROI that combines CC and occipital white matter (15 voxels; see Results section for details). All plots were obtained by using a surface mesh with 10 000 points distributed

evenly in the polar coordinate. Two viewing angles, one from the posterior side and the other from the right side are shown for all angular plots unless otherwise specified. To illustrate the variation between different repetitions, two surfaces are shown in each angular plot: an inner opaque one showing mean $-$ SD and an outer transparent one showing mean $+$ SD over the three repetitions.

Spherical harmonics expansion was performed using numerical integration. Different orders of the coefficients, A_{lm} (0th, 2nd and 4th order), were computed and the power indices, C_0 , C_2 , C_4 were also calculated. To obtain typical values of C_i , ROIs were selected in the following brain structures using ImageJ (National Institutes of Health, Bethesda, MD, USA): gray matter, ROI size 4.8 ± 0.4 ($n = 4$, mean \pm SEM) voxels; white matter, ROI size 9.0 ± 0.6 voxels; thalamus, ROI size 6.0 ± 0.0 voxels.

RESULTS

Figure 1 shows an example of the fitting results in an ROI containing CC for four representative gradient directions. A nonlinear signal decay of the logarithm of the MR signal can be clearly seen, suggesting non-Gaussian water diffusion. Such fitting results were routinely obtained for our data. Figure 2(a) shows the AKC maps in 30 directions for one slice. The kurtosis in white matter regions varies dramatically for different gradient directions, whereas the kurtosis in gray matter is less dependent on the gradient directions. Figure 2(b–d) illustrates the average AKC map, ADC trace map and FA map, respectively. Clear contrast can be seen between gray matter and white matter in the average AKC map. This is different from the mean diffusivity map, which shows a very small difference between gray and white matter. It should be noted that the average AKC, an equivalent of the mean ADC index for DTI, is simply an average of the 30 maps in Fig. 2a and does not reflect the anisotropy of the tissue.

Figure 2(e–g) shows the results of spherical harmonics expansion. The harmonic power index, C , indicates the

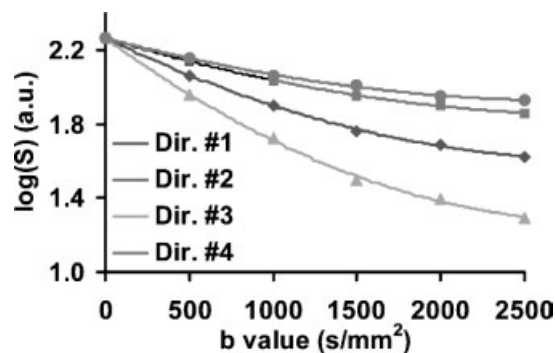


Figure 1. Logarithm of MR signal vs b values at four gradient directions in an ROI containing corpus callosum. The symbols represent experimental data, and the solid lines are fitted curves. Nonlinear decay is seen in all directions.

distribution of the power in different spatial frequencies. C_0 can be analytically shown to be equal to the mean kurtosis averaged over all angular directions. With a sufficiently large number of measurement directions, C_0 is almost identical to the average AKC map [comparing Fig. 2(b) and (e)]. C_2 and C_4 reflect the power of higher spatial frequencies. The image contrast of the C_2 map appears to be similar to that of FA map from DTI. However, when comparing C_2 and C_4 , one can see a dark band [arrow in Fig. 2(f)] in the C_2 map but not in the C_4 map. This difference was consistently observed for all repetitions. Interestingly, the location of this band coincides with the well-known anatomy of fiber crossing between internal capsule and fronto-occipital fasciculus (36). We believe that, owing to nearly perpendicular crossing of two fibers, the FA (as well as C_2) in the voxel is significantly reduced and thereby exhibits a very small value. The C_4 index, however, contains higher frequency components and can preserve the anisotropy information. Note also that the C_2 and C_4 maps contain more pronounced artifacts in brain boundaries [e.g. lower left regions in Fig. 2(f) and (g)], suggesting that the kurtosis estimation is more sensitive to motion compared with DTI. Table 1 lists the C values for different brain regions. It was found that $C_{0,white} > C_{0,thalamus}$, $C_{0,white} > C_{0,gray}$ (paired Student t -test, two tailed, $p < 0.005$). $C_{0,thalamus}$ is slightly higher than $C_{0,gray}$, but the p -value ($p = 0.059$) is just above our significance threshold of $p < 0.05$. Note that the spherical harmonics expansion reduces the four-dimensional matrix into simple indices, allowing easier comparison of diffusion kurtosis between different brain regions or in the same brain regions amongst different patient groups. Figure 3(a–c) shows the scatter plots between the FA and the kurtosis parameters, C_0 , C_2 and C_4 , respectively. The cross correlation coefficients were found to be 0.125, 0.198 and 0.162 for the three plots, respectively.

Our reproducibility study shows that the variation across trials, defined as the ratio between the standard deviation and the mean, is 2.3 ± 2.3 , 10.0 ± 7.7 and $14.1 \pm 10.2\%$ for C_0 , C_2 and C_4 , respectively. It can be seen that C_0 (or average AKC) is relatively robust and the higher-order indices are more variable. The inclusion of a noise term [i.e. η in Jensen *et al.* (27)] in the model did not affect the precision of the results, giving very similar variations across trials. However, a small but systematic difference is seen between the averaged values. The difference, defined as $(C_{i, without} - C_{i, with})/C_{i, with}$, was found to be 1.9 ± 2.8 , -1.4 ± 4.4 , $-2.9 \pm 8.6\%$ for C_0 , C_2 and C_4 , respectively. The AKC is elevated when no noise term is included, because the signal decay may artifactually deviate from a linear curve when the signal is close to the noise level.

Aside from the effects described above, noise can introduce another source of error, because fitting a nonlinear model in the presence of noise can result in biased estimations. Numerical simulations that included

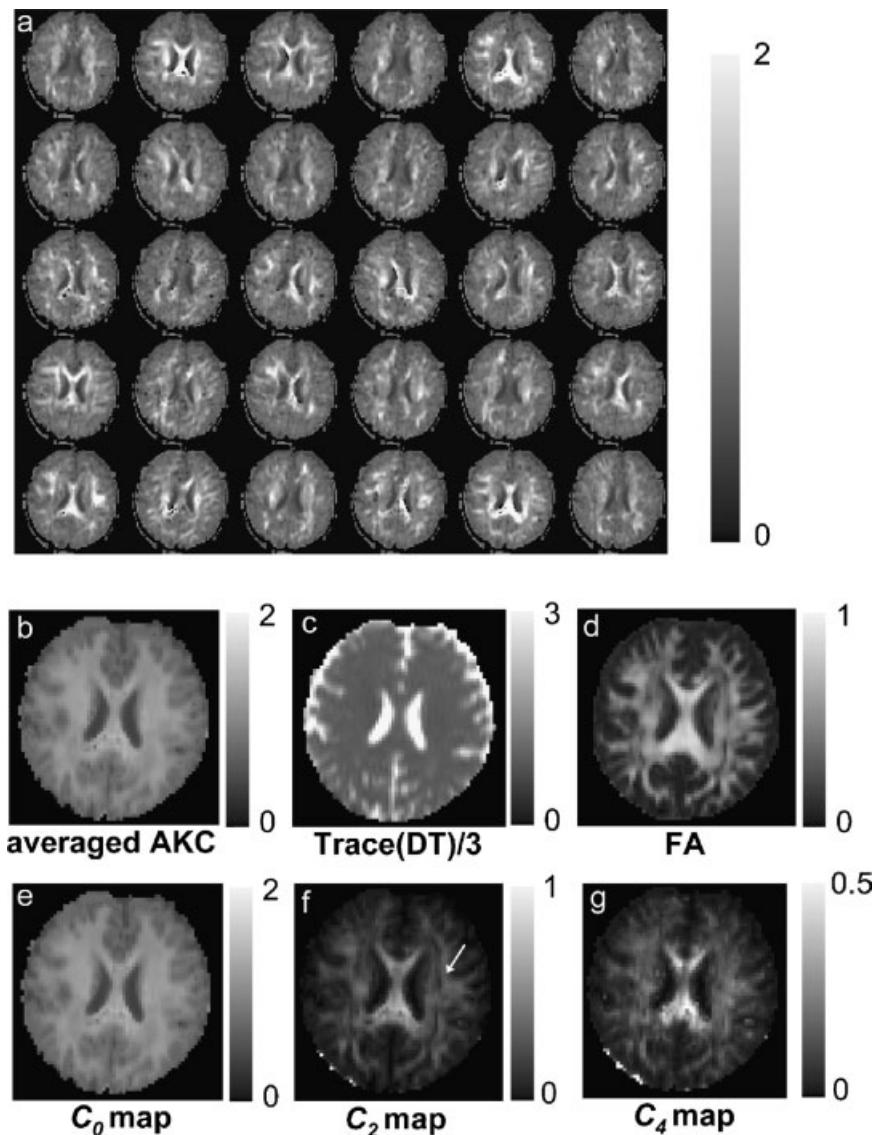


Figure 2. (a) AKC map for 30 gradient directions in one slice. (b) Average (over 30 directions) AKC map. (c) Trace(DT)/3 map. (d) FA map. (e–g) Results from the spherical harmonics expansion: C_0 (e), C_2 (f) and C_4 (g) maps. They represent the decomposition of the kurtosis angular structure into different frequency components. The unit for the scale bar is $\mu\text{m}^2/\text{ms}$ for Trace(DT)/2 map and is dimensionless for the other maps. C_0 represents the mean AKC averaged over all angular directions. Notice the presence of a dark band in the middle of white matter (arrow) in the C_2 map but not in the C_0 and C_4 map. We believe that this is not due to a white matter lesion, but rather because of fiber crossings between internal capsule and fronto-occipital fasciculus. Note the different scale bars for the three maps.

variable amplitudes of noise showed that the kurtosis values are under-estimated by 2, 11 and 59% when the SNR in the b_0 image is 40, 20 and 12, respectively. It should be noted that this effect cannot be corrected by including the noise term in the model, and will be present even if complex image data are acquired.

The application of spatial filtering was found to improve the accuracy of the kurtosis estimation. The results using unfiltered data had considerably higher variations between trials, giving $5.2 \pm 19.1\%$ for averaged AKC, which is approximately twice the value with

the filtered data. Note that, however, spatial filtering decreases the effective spatial resolution in the results.

Figure 4(a) shows an ROI in the CC, the fiber direction of which is known to be left–right. Figure 4(b) and (c) shows the angular plot of the DT from two different viewing angles (viewing from posterior for b; viewing from the right for c). As previously shown (15,17), the DT angular plot is dumb-bell shaped with the principal axis in the left–right direction for CC. The angular plot for kurtosis [Fig. 4(d) and (e)], on the other hand, shows dramatically different characteristics. It appears to exhibit

Table 1. Parameters of kurtosis and diffusion in normal volunteers ($n = 4$, mean \pm SEM)

	Gray matter (4.8 ± 0.4 voxels)	White matter (9.0 ± 0.6 voxels)	Thalamus (6.0 ± 0.0 voxels)
C_0 (mean AKC)	0.74 ± 0.03	1.09 ± 0.01	0.84 ± 0.02
Mean ADC ($\mu\text{m}^2/\text{ms}$)	1.00 ± 0.06	0.90 ± 0.02	0.95 ± 0.03
C_2	0.07 ± 0.01	0.30 ± 0.02	0.09 ± 0.01
C_4	0.07 ± 0.01	0.19 ± 0.03	0.08 ± 0.01
FA	0.17 ± 0.03	0.55 ± 0.04	0.27 ± 0.02

a pancake-shaped structure. The kurtosis along the fiber direction is very small, consistent with the expectation that the water diffusion is less hindered or restricted. The cross-sectional directions, however, show high kurtosis, presumably due to the axonal membrane and/or myelin restriction, causing the displacement distribution function to significantly deviate from a perfect Gaussian curve. It can also be seen that the angular plots for the kurtosis are in general agreement among different trials, showing only small differences between the opaque and the transparent surfaces.

Figure 4(f) illustrates the results of angular plot as a function of number of voxels. The ratios between standard deviation and mean (averaged over all angular directions) are 4.0, 4.0, 4.1, 4.5, 4.7, 5.4 and 4.9% for the seven scenarios [Fig. 4(f)], respectively. A larger number of voxels results in reduced level of variation among trials. However, it can be seen that the general structure of the angular plot is maintained even at a single-voxel resolution.

Figure 5(a) and (b) shows the kurtosis angular plot for the asparagus phantom, further demonstrating the kurtosis characteristics of an object that contains single direction fibers. Figure 5(c) and (d) illustrates the Monte-Carlo simulation results for a single fiber structure using models similar to Liu *et al.* (17). It is clear that our results from both the asparagus phantom and the human white matter are qualitatively consistent with the simulation predictions.

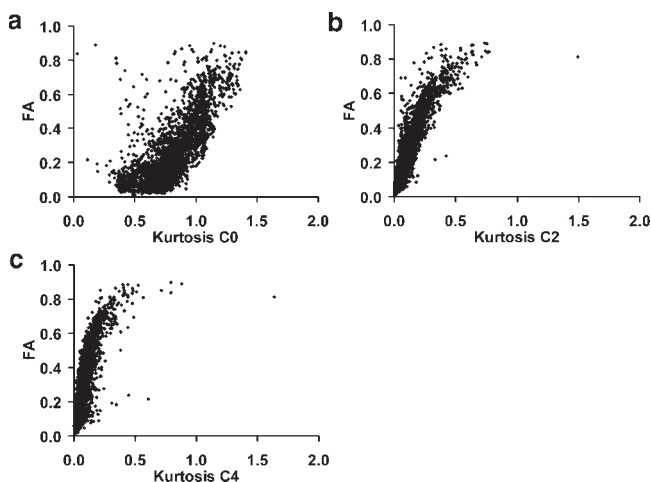


Figure 3. Scatter plots between (a) C_0 and FA, (b) C_2 and FA, (c) C_4 and FA. The plots include 2933 voxels taken from one slice. All parameters are dimensionless.

Figure 6 shows the kurtosis angular plots for gray matter (a and b) and occipital white matter (c and d). The kurtosis plot in the gray matter region is nearly spherical with a small amplitude. The fiber orientation in the occipital white matter ROI is anterior–posterior. Consequently, the kurtosis angular plot shows a pancake-shaped structure with a principal axis orthogonal to that of the CC.

Since the DK tensor has a higher degree of freedom (15 independent elements) compared with DT (six independent elements), it imposes fewer restrictions on the geometry of the angular plot and can potentially provide more information than the conventional DT. This can be illustrated using the case of crossing fiber identification. We studied a synthetic voxel, in which we added the raw data (signals at $b = 0$, $b = 500$, \dots , $b = 2500 \text{ s/mm}^2$) of the corpus callosum ROI to the raw data of the occipital white matter ROI in a pair-wise manner to a ‘new’ voxel whose signals are:

$$S_{\text{synthetic}, b=0} = S_{\text{cc}, b=0} + S_{\text{owm}, b=0}, \quad S_{\text{synthetic}, b=500} = S_{\text{cc}, b=500} + S_{\text{owm}, b=500},$$

etc. This can be used to simulate the situation of a crossing fiber voxel. Then the DTI and DKI processing were conducted for this voxel (30 directions and six b values for each direction). Figure 7(a) shows the angular plot for diffusion (upper row) and kurtosis (lower row) from two different viewing angles. It can be seen that the DK structure of the synthetic fiber appears to be a superposition of the two kurtosis angular plots [see Figs. 4(d, e) and (c, d)] from the individual ROIs, showing features of two orthogonal fibers. On the other hand, the DT structure does not exhibit crossing fiber characteristics, and its shape is similar to that of a single oblique fiber. This is because the DT angular plot can only assume certain geometric shapes and any higher degree geometry will be filtered out, creating a ‘smoothing’ effect on the surface plot.

To further validate this, a phantom experiment was conducted in which two halves of an asparagus were glued together in perpendicular fiber orientations, and an ROI (15 voxels) containing parts of both halves was selected for DK analysis. The results are shown in Fig. 7(b), giving similar shapes as the synthetic fiber. These observations indicate that the DK angular plot of multiple fibers shows different characteristics from that of a single fiber, and this feature may be used to obtain the underlying multi-fiber information using methods similar

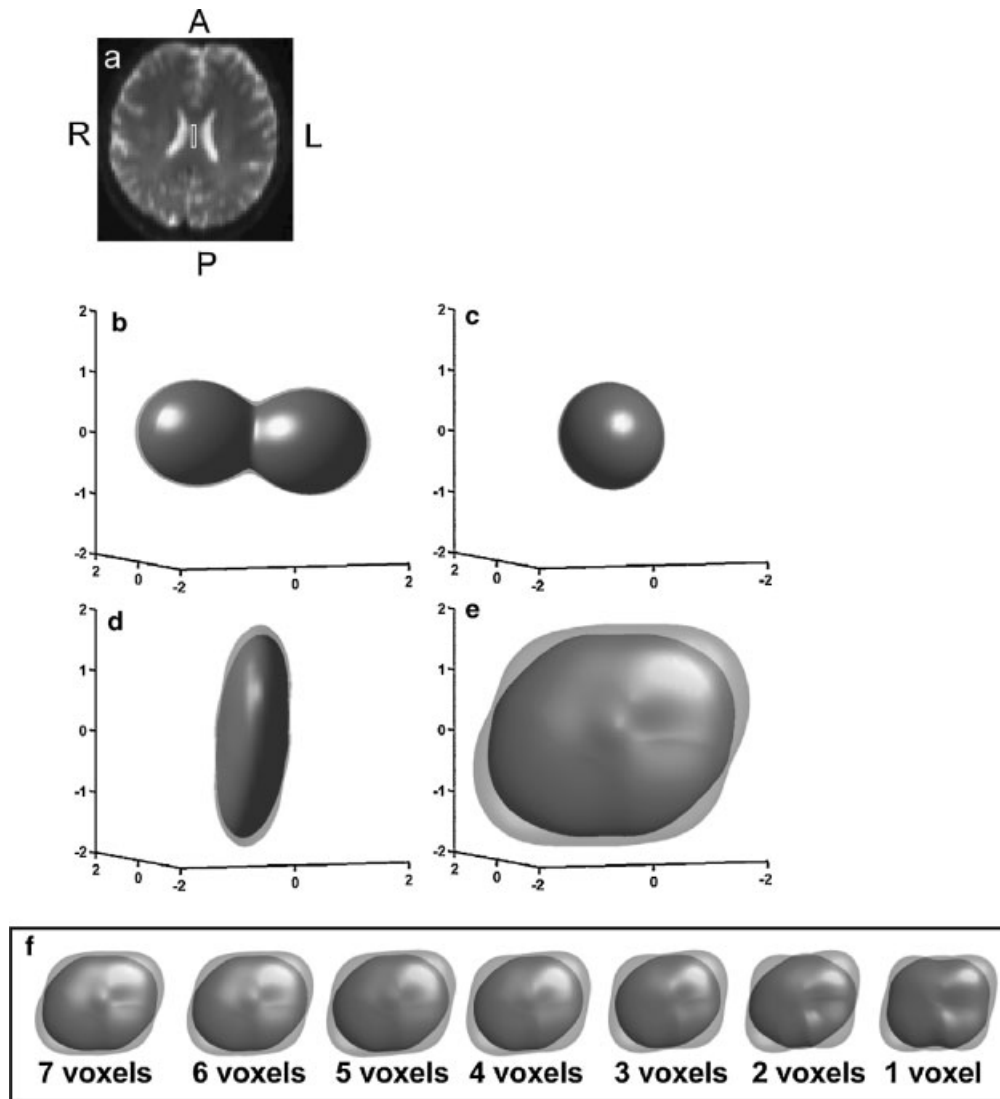


Figure 4. (a) An ROI (seven voxels) containing corpus callosum. A, anterior; P, posterior; R, right; L, left. (b–e) Angular plot of diffusion and kurtosis in the ROI. Left column: view from posterior side; right column: view from right side. To illustrate the variation between different repetitions, two surfaces are shown in each angular plot: an inner opaque one showing mean – SD and an outer transparent one showing mean + SD over the three repetitions. (b, c) Diffusion angular plot. (d, e) Kurtosis angular plot. (f) Angular plot as a function of voxel number. The seven voxels in the entire ROI were removed one-by-one and the remaining voxels were analyzed for the DK angular plot. One viewing angle from the right side is shown.

to that proposed by Tournier *et al.*(37). To localize potential regions that contain fiber crossings, one can combine the FA and the kurtosis C_0 information. As shown in Fig. 7(c), the voxels of gray matter, regular white matter and fiber-crossing white matter form separate clusters in the two-dimensional plot, which cannot be achieved using each parametric map alone. This type of separation could not be achieved by using the FA and ADC maps owing to a lack of gray-white contrast in the ADC map. Figure 7(d) shows an example of the voxel sorting results using FA and C_0 . Voxels that may contain multiple fiber directions are coded in green.

DISCUSSION

In this study, a new technique is proposed to measure the non-Gaussian behavior of the water diffusion, characterized by a diffusion kurtosis tensor, in humans within a clinically feasible time of approximately 10 min. The results were found to be robust and reproducible. Kurtosis values for typical brain regions have been established. Methods to visualize the 3D kurtosis characteristics have been developed. Several useful indices for the kurtosis tensor are also presented.

Non-Gaussian behavior of the water diffusion has been noted previously (12–15,17) and the kurtosis of the

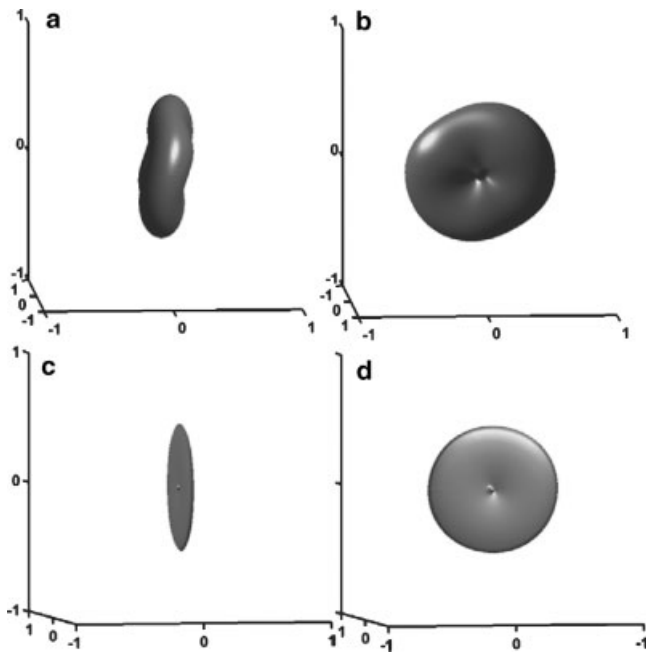


Figure 5. (a, b) Kurtosis angular plot of an asparagus phantom. Two viewing angles are shown, similar to Fig. 4. The asparagus was placed in left-right orientation. (c, d) Monte-Carlo simulation results for a single fiber oriented in left-right orientation. Simulation parameters: fiber diameter $10\ \mu\text{m}$, free-diffusion ADC $2.02\ \mu\text{m}^2/\text{ms}$, diffusion time $104\ \text{ms}$, time step $0.2\ \text{ms}$, number of samples $70\ 000$.

displacement distribution function has been determined in a limited number of directions (27,38,39). Here, for the first time, we demonstrate the feasibility of measuring the 3D property of the diffusion kurtosis in humans on a clinical MR system. This is because our technique aims at the direct measurement of kurtosis values (27), rather than

using a q -space imaging approach for which the displacement distribution function must first be determined prior to calculating the kurtosis (38,39). Therefore, our method requires fewer b values and is more time-efficient for kurtosis estimation, even though it does not provide other aspects of the displacement distribution function that q -space imaging provides (18).

The information contained in the DK tensor is, by definition, different and complementary to that in the conventional DT. The DT describes the diffusion distance averaged over all water spins in the voxel, whereas the diffusion kurtosis enables one to probe the deviation of water transport from homogeneous, unrestricted, free diffusion. In many situations, increases in DK are accompanied by decreases in ADC. However, this need not always be the case. For instance, when the viscosity of the media is higher, the ADC will decrease but the DK will remain the same (27). In the brain, the image contrast of the mean AKC maps, i.e. C_0 map [Fig. 2(e)], was found to be dramatically different from the DT parameters, such as Trace(DT) or FA maps. The 3D angular plots of the DK tensor have a higher degree of freedom than those obtained from conventional DTI, and therefore can undertake more variable geometric shapes. As a result, they are capable of representing more complex structures, an advantage similar to that offered by HARDI (15,21) or q -ball imaging (20,35). Such a feature is useful for identification of crossing fibers (Fig. 7) and may be applied in DT tractography algorithms.

As discussed, the diffusion kurtosis measured in this study considers the diffusion distance of all water molecules in the voxel and reflects how much the displacement distribution function of these molecules deviate from a perfect Gaussian function. As a result, a non-zero kurtosis value may originate from a single-compartment-voxel with diffusion barriers or from a multiple-compartment-voxel in which each compartment has perfect Gaussian diffusion, but the diffusion constants in different compartments are different. Therefore, some care should be exercised in assigning specific physical origins to observed kurtosis differences.

The nonlinear fitting based on the Levenberg–Marquardt algorithm was found to converge robustly and the results were not sensitive to the initial values used in the iterative process. This is probably due to the fact that the kurtosis model is relatively simple and the number of fitting parameters is limited to three. The overall precision of our diffusion kurtosis estimation is high, showing reproducible results for both kurtosis angular plots (Fig. 4) and DKI maps, e.g. C_0 , C_2 , C_4 (data not shown). Our kurtosis values are in general agreement with the values reported in literature (27,38,39). However, a quantitative comparison with the literature values is difficult since the diffusion kurtosis is dependent on the scale of the diffusion displacement and therefore on the echo time used. Our fitting procedure generates robust parameter estimations for most of the voxels and directions. However, it can also

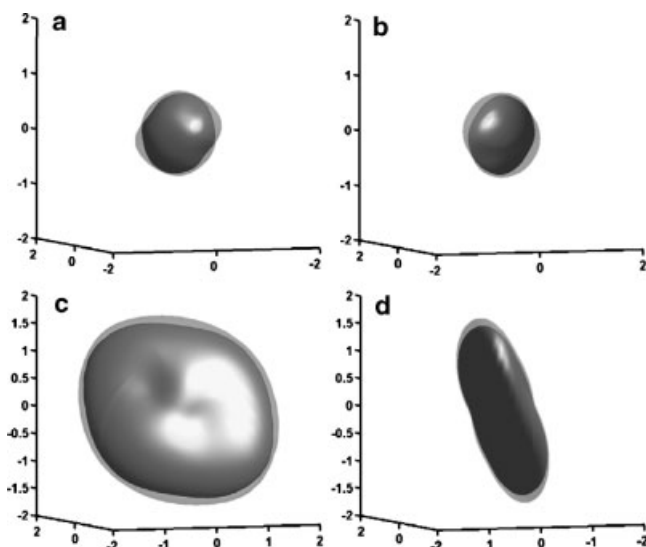


Figure 6. Kurtosis angular plots in ROI containing GM (a, b), occipital WM (c, d) (fiber AP orientation). Two viewing angles are shown. Number of voxels in ROI: four to eight voxels.

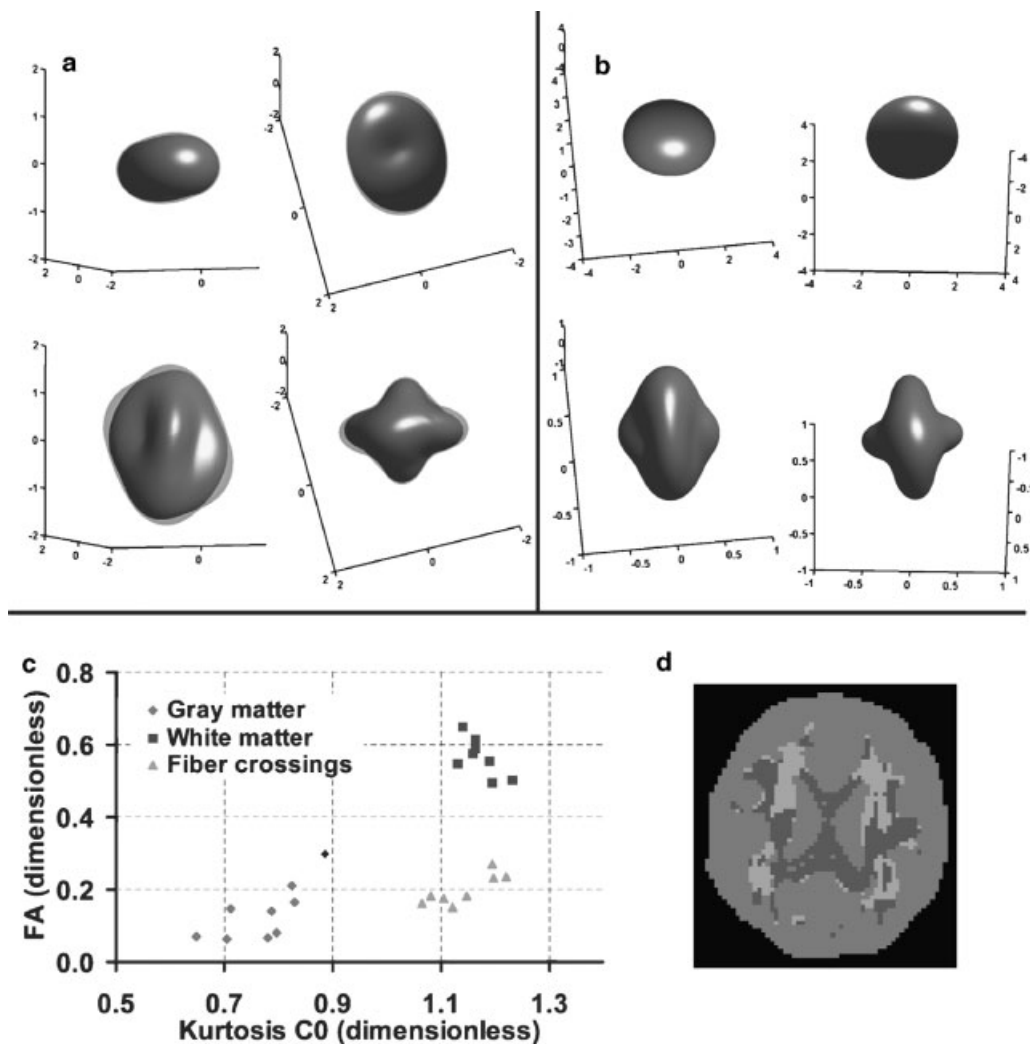


Figure 7. (a) Diffusion (upper row) and Kurtosis (lower row) angular plots for a synthetic voxel that was obtained by combining the raw data of CC and occipital WM, creating a pre-defined crossing fiber situation. Presence of multiple fibers can be clearly seen in kurtosis plots but not in DT plots. Two viewing angles are shown. (b) Experimental results from a phantom that contains two halves of perpendicularly positioned asparagus. Two-fiber characteristics can be clearly seen in the kurtosis plot. (c) Scatter plot of kurtosis and FA values in three representative regions from a normal volunteer: gray matter (nine voxels), white matter without fiber-crossing (eight voxels), white matter with possible fiber-crossings (eight voxels). Combination of both parametric maps allows the identification of possible fiber-crossing regions, for which the kurtosis angular plot may be decomposed into multiple components. (d) An example of voxel sorting results using FA and C_0 as the indices. Red: voxels that have low C_0 values; blue: voxels that have high FA and high C_0 values; green: voxels that have low FA and high C_0 values. The green voxels may contain multiple fiber directions. FA threshold: 0.4. C_0 threshold: 1.0.

be seen that some voxels [Fig. 2(a)] in the DKI maps are unusually dark, which is due to ill-conditioned fitting results. This often occurs in situations where the signal decay as a function of the b value is very small and the dynamic range of the data is limited.

The current study used a total of six b values with the maximum b value of 2500 s/mm^2 . We have tested the use of a subset of the data and compared the results with those from the whole dataset. We calculated the 95% confidence interval of the AKC on a voxel-by-voxel basis for all encoding directions. The interval values were

then averaged over the 30 directions and normalized against the mean AKC values. It was found that the normalized confidence interval was 0.56 ± 0.76 , 1.04 ± 2.47 and 5.23 ± 67.97 for the results using six, five and four b values, respectively. Based on this analysis, we recommend that a minimum of five b values should preferably be used. In terms of the maximum b value, our simulation using typical parameters ($\text{ADC} = 1 \mu\text{m}^2/\text{ms}$, $\text{AKC} = 1$) shows that the quadratic approximation would no longer be valid (i.e. higher order components are not negligible) when the b value was

3000 s/mm² or larger. Therefore, the maximum b value should be limited to within about 3000 s/mm². As shown in the Results section, the noise can cause an underestimation in the fitting results. Thus, we recommend that DKI should be conducted only when the SNR in the b_0 image is at least 20. For the protocol used in the current study, the SNR was found to be above 40 in all subjects. When the SNR is above 20, simulations show that larger b values tend to provide more accurate estimations of the kurtosis values. We recommend a maximum b value of 2000–2500 s/mm² for typical DKI acquisitions. In this study, 30 diffusion encoding directions were used in the experiments for a tradeoff between scan duration and accuracy of the parameter estimation. In principle, a larger number of encoding directions (e.g. 60 directions) will improve the estimation of the kurtosis tensor. On the other hand, longer scan duration may not be well tolerated in clinical applications and, even tolerated, greater motion artifacts may occur. Our data suggest that the kurtosis parametric maps are highly reproducible using the 30 encoding directions. However, further study is needed to investigate the effect of number of directions on the kurtosis tensor matrix and the optimal choices of the b directions for a given scan duration.

The current study uses the software SPM for three-dimensional motion correction. To evaluate the effectiveness of the motion correction algorithm on our data and how the residual motion affects the kurtosis estimation, one dataset with minimal motion was selected as a motion-free template and simulations were performed to generate random motions: for each volume in the dataset (containing three b_0 volumes, $30 \times 5 = 150$ diffusion-weighted volumes), three translational parameters (t_x , t_y and t_z) and three rotational parameters (r_x , r_y and r_z) were generated using a random-number generation script. Each parameter has a Gaussian probability density distribution with zero mean and a fixed value of standard deviation. The spatial transformation with these six parameters is then applied to the volume using a SPM reslicing script (using B-spline interpolation). Four simulations were conducted with different amplitudes of translation and rotation (i.e. standard deviations of the Gaussian distribution): rotation 1°, translation 1 mm; rotation 2°, translation 2 mm; rotation 4°, translation 4 mm; rotation 8°, translation 8 mm. Then the motion correction algorithm was applied and the detected rotation and translation values were compared to the true values. It was found that the algorithm can correct well for the images with identical contrast (e.g. b_0 image with another b_0 image), but was not satisfactory in correcting for images with different b values or b directions. When using the algorithm to co-register the b_0 images with the simulated motion described above, the residual errors after correction were found to be 24.3 ± 4.7 (a.u.), 25.5 ± 3.0 , 26.7 ± 1.0 , 37.8 ± 17.7 , respectively. Note that the increased residual errors for the data with 8° of rotation and 8 mm of translation may

be attributed to the imperfect interpolation when generating the 'motion' data, rather than due to the motion correction algorithm. The impact of motion on the averaged kurtosis map was found to be mainly a smoothing effect, causing the map to be blurred. In this study, the acquisitions of b_0 images were spread within the sequence, namely one at the very beginning, one after 12 b directions, and one after 18 b directions. The motion correction algorithm was applied to each pair of b_0 images, and the resulting transformation was applied to all images following that b_0 . It should be kept in mind that any motion occurred during acquisitions of non-zero b values will remain in the data.

It is important to point out that the data acquired using our DKI protocol contains the data needed for conventional DT calculation. That is, the DTI data is a subset of the DKI data. Since the DK data fitting [second-order polynomial between $\log(s)$ and b values; see equation (1)] results in both AKC and ADC, we compared the ADC values obtained using the DK model to that using the conventional monoexponential model [fitting of a straight line between $\log(s)$ and b values]. Since DTI studies usually use two b values, one b value of zero and the other b value ranging between 500 and 1000 s/mm², we selected two b values from our DKI dataset. Two cases were tested, in one case b of 0 and 500 s/mm² and in the other case b of 0 and 1000 s/mm². It was found that the ADC estimated using the monoexponential model was systematically lower ($p < 0.05$) than that from the kurtosis model (second-order polynomial). The discrepancy is smaller for lower b values: $6.1 \pm 4.7\%$ when b values of 0 and 500 s/mm² were used; $14.5 \pm 2.9\%$ when b values of 0 and 1000 s/mm² were used. We believe this is because the second-order polynomial fitting would always provide better fitting results than that from a linear curve fitting. However, when the range of b values is small, the experimental data is close to a linear curve, and the two fittings (linear curve and second-order curve) will yield similar results. Therefore, it is expected that the results using the second-order polynomial model can provide a more accurate estimation of the true ADC.

The spherical harmonics expansion is a useful method to reduce any 3D angular plot to simple indices (15,34), and allows quantitative comparison between two angular plots. This method decomposes a given plot into the summation of a series of basis functions, and each basis function reflects a different frequency component. For a perfect sphere, the spherical harmonics expansion gives a nonzero coefficient for the 0th order harmonic and all other higher order coefficients vanish. For a structure that is specified by a fully symmetric 3×3 matrix, as in the case of a conventional DT, the series truncates after the 2nd order harmonic (15). Similarly, an angular structure that is specified by a fully symmetric $3 \times 3 \times 3$ matrix would truncate after the 4th order harmonic. Note, however, that the DK angular plot is not a simple

directional evaluation of the $3 \times 3 \times 3 \times 3$ matrix, W_{ijkl} . Instead, the AKC in a given direction is also affected by the ADC value [see equation (2)]. As a result, the expansion of the kurtosis angular plot does not truncate at the 4th order. However, the number of independent variables is limited to 15, assuming the DT is known. That is, the coefficients of higher orders can be calculated from the lower order coefficients.

Our previous paper (27) was mainly focused on establishing the theoretical framework of diffusion kurtosis and how this parameter can be measured using MRI. In this study, our efforts were concentrated on the implementation of this technique and the related pragmatic issues, including optimal imaging parameters, signal-to-noise ratio, motion effects and potential applications. The goal is to establish an optimized protocol that can provide sufficient signal-to-noise within a reasonable scan time. We have now shown how to determine the full diffusion kurtosis tensor on a clinical MR system with a scan duration of approximately 10 min, which makes the method feasible for clinical studies.

We can consider q -space imaging as a 'gold standard' for completely describing the water diffusion behavior. If diffusion tensor imaging is a first-order approximation, then diffusion kurtosis imaging is a second-order approximation. Our results show that diffusion kurtosis imaging only modestly increases the scan duration and MR hardware requirements, and yet it can provide additional, useful information regarding tissue microstructural complexity and directional anisotropy. Generalized diffusion tensors have been employed by Özarslan and Mareci in order to assess high angular resolution diffusion imaging (HARDI) data (24). Their formalism differs from the one presented here in several respects. First, the diffusion coefficient in a given direction is obtained from a monoexponential fit to the signal intensity data, rather than the non-monoexponential form of equation (1). Second, the generalized diffusion tensors defined by Özarslan and Mareci are dependent on the choice of b value, while the tensors given by equation (2) are not. Third, their approach would not yield any information beyond the ADC for isotropic tissues.

CONCLUSION

The non-Gaussian property of water diffusion in brain can be quantified by the proposed DKI technique. A DKI experiment can be performed on a clinical scanner with an acquisition time of approximately 10 min. The results show tissue-specific kurtosis characteristics in different brain regions. It is shown that the diffusion kurtosis contains additional and complementary information compared with the conventional diffusion tensor.

APPENDIX

Simplification of equation (2) to compute the DK tensor from individual AKC values

Considering the symmetry of the DK tensor, equation (2) can be rewritten as: (A1)

$$\begin{aligned} \frac{K_{\text{app}} \cdot D_{\text{app}}^2}{M_D^2} = & n_1^4 \cdot W_{1111} + n_2^4 \cdot W_{2222} + n_3^4 \cdot W_{3333} \\ & + 4n_1^3 n_2 W_{1112} + 4n_1^3 n_3 W_{1113} + 4n_1 n_2^3 \cdot W_{1222} \\ & + 4n_2^3 n_3 W_{2223} + 4n_1 n_3^3 \cdot W_{1333} + 4n_2 n_3^3 \cdot W_{2333} \\ & + 6n_1^2 n_2^2 W_{1122} + 6n_1^2 n_3^2 W_{1133} + 6n_2^2 n_3^2 W_{2233} \\ & + 12n_1^2 n_2 n_3 W_{1123} + 12n_1 n_2^2 n_3 W_{1223} \\ & + 12n_1 n_2 n_3^2 W_{1233} \end{aligned}$$

This is a linear equation that can be used to solve the DK tensor, W_{ijkl} .

REFERENCES

1. Moseley ME, Cohen Y, Kucharczyk J, Mintorovitch J, Asgari HS, Wendland MF, Tsuruda J, Norman D. Diffusion-weighted MR imaging of anisotropic water diffusion in cat central nervous system. *Radiology* 1990; **176**: 439–445.
2. Basser PJ, Mattiello J, LeBihan D. MR diffusion tensor spectroscopy and imaging. *Biophys. J.* 1994; **66**: 259–267.
3. Basser PJ, Mattiello J, LeBihan D. Estimation of the effective self-diffusion tensor from the NMR spin echo. *J. Magn. Reson. B* 1994; **103**: 247–254.
4. Le Bihan D. Molecular diffusion, tissue microdynamics and microstructure. *NMR Biomed.* 1995; **8**: 375–386.
5. Pierpaoli C, Jezzard P, Basser PJ, Barnett A, Di Chiro G. Diffusion tensor MR imaging of the human brain. *Radiology* 1996; **201**: 637–648.
6. Mori S, Crain BJ, Chacko VP, van Zijl PC. Three-dimensional tracking of axonal projections in the brain by magnetic resonance imaging. *Ann. Neurol.* 1999; **45**: 265–269.
7. Conturo TE, Lori NF, Cull TS, Akbudak E, Snyder AZ, Shimony JS, McKinstry RC, Burton H, Raichle ME. Tracking neuronal fiber pathways in the living human brain. *Proc. Natl Acad. Sci. USA* 1999; **96**: 10422–10427.
8. Knight RA, Ordidge RJ, Helpert JA, Chopp M, Rodolosi LC, Peck D. Temporal evolution of ischemic damage in rat brain measured by proton nuclear magnetic resonance imaging. *Stroke* 1991; **22**: 802–808.
9. Basser PJ, Jones DK. Diffusion-tensor MRI: theory, experimental design and data analysis – a technical review. *NMR Biomed.* 2002; **15**: 456–467.
10. Niendorf T, Norris DG, Leibfritz D. Detection of apparent restricted diffusion in healthy rat brain at short diffusion times. *Magn. Reson. Med.* 1994; **32**: 672–677.
11. King MD, Houseman J, Roussel SA, van Bruggen N, Williams SR, Gadian DG. q -Space imaging of the brain. *Magn. Reson. Med.* 1994; **32**: 707–713.
12. Niendorf T, Dijkhuizen RM, Norris DG, van Lookeren Campagne M, Nicolay K. Biexponential diffusion attenuation in various states of brain tissue: implications for diffusion-weighted imaging. *Magn. Reson. Med.* 1996; **36**: 847–857.
13. Mulkern RV, Gudbjartsson H, Westin CF, Zengingonul HP, Gartner W, Guttman CR, Robertson RL, Kyriakos W, Schwartz R, Holtzman D, Jolesz FA, Maier SE. Multi-component apparent

- diffusion coefficients in human brain. *NMR Biomed.* 1999; **12**: 51–62.
14. Clark CA, Le Bihan D. Water diffusion compartmentation and anisotropy at high b values in the human brain. *Magn. Reson. Med.* 2000; **44**: 852–859.
 15. Alexander DC, Barker GJ, Arridge SR. Detection and modeling of non-Gaussian apparent diffusion coefficient profiles in human brain data. *Magn. Reson. Med.* 2002; **48**: 331–340.
 16. Assaf Y, Freidlin RZ, Rohde GK, Basser PJ. New modeling and experimental framework to characterize hindered and restricted water diffusion in brain white matter. *Magn. Reson. Med.* 2004; **52**: 965–978.
 17. Liu C, Bammer R, Acar B, Moseley ME. Characterizing non-Gaussian diffusion by using generalized diffusion tensors. *Magn. Reson. Med.* 2004; **51**: 924–937.
 18. Callaghan PT. *Principles of Nuclear Magnetic Resonance Microscopy*. Oxford University Press: Oxford, 1993.
 19. Assaf Y, Cohen Y. Structural information in neuronal tissue as revealed by q-space diffusion NMR spectroscopy of metabolites in bovine optic nerve. *NMR Biomed.* 1999; **12**: 335–344.
 20. Tuch DS, Reese TG, Wiegell MR, Wedeen VJ. Diffusion MRI of complex neural architecture. *Neuron* 2003; **40**: 885–895.
 21. Frank LR. Anisotropy in high angular resolution diffusion-weighted MRI. *Magn. Reson. Med.* 2001; **45**: 935–939.
 22. Lin CP, Wedeen VJ, Chen JH, Yao C, Tseng WY. Validation of diffusion spectrum magnetic resonance imaging with manganese-enhanced rat optic tracts and ex vivo phantoms. *Neuroimage* 2003; **19**: 482–495.
 23. Maier SE, Vajapeyam S, Mamata H, Westin CF, Jolesz FA, Mulkern RV. Biexponential diffusion tensor analysis of human brain diffusion data. *Magn. Reson. Med.* 2004; **51**: 321–330.
 24. Ozarslan E, Mareci TH. Generalized diffusion tensor imaging and analytical relationships between diffusion tensor imaging and high angular resolution diffusion imaging. *Magn. Reson. Med.* 2003; **50**: 955–965.
 25. Liu C, Bammer R, Moseley ME. Limitations of apparent diffusion coefficient-based models in characterizing non-gaussian diffusion. *Magn. Reson. Med.* 2005; **54**: 419–428.
 26. Topgaard D, Soderman O. Experimental determination of pore shape and size using q-space NMR microscopy in the long diffusion-time limit. *Magn. Reson. Imag.* 2003; **21**: 69–76.
 27. Jensen JH, Helpert JA, Ramani A, Lu H, Kaczynski K. Diffusional kurtosis imaging: the quantification of non-Gaussian water diffusion by means of MRI. *Magn. Reson. Med.* 2005; **53**: 1432–1440.
 28. Balanda KP, MacGillivray HL. Kurtosis: a critical review. *Am. Stat.* 1988; **42**: 111–119.
 29. Jackson JD. *Classical Electrodynamics*. Wiley: New York, 1975.
 30. Reese TG, Heid O, Weisskoff RM, Wedeen VJ. Reduction of eddy-current-induced distortion in diffusion MRI using a twice-refocused spin echo. *Magn. Reson. Med.* 2003; **49**: 177–182.
 31. Jones DK, Horsfield MA, Simmons A. Optimal strategies for measuring diffusion in anisotropic systems by magnetic resonance imaging. *Magn. Reson. Med.* 1999; **42**: 515–525.
 32. Skare S, Hedehus M, Moseley ME, Li TQ. Condition number as a measure of noise performance of diffusion tensor data acquisition schemes with MRI. *J. Magn. Reson.* 2000; **147**: 340–352.
 33. Bates DM, Watts DG. *Nonlinear Regression Analysis and its Applications*. Wiley: New York, 1988.
 34. Frank LR. Characterization of anisotropy in high angular resolution diffusion-weighted MRI. *Magn. Reson. Med.* 2002; **47**: 1083–1099.
 35. Tuch DS. Q-ball imaging. *Magn. Reson. Med.* 2004; **52**: 1358–1372.
 36. Wakana S, Jiang H, Nagae-Poetscher LM, van Zijl PC, Mori S. Fiber tract-based atlas of human white matter anatomy. *Radiology* 2004; **230**: 77–87.
 37. Tournier JD, Calamante F, Gadian DG, Connelly A. Direct estimation of the fiber orientation density function from diffusion-weighted MRI data using spherical deconvolution. *Neuroimage* 2004; **23**: 1176–1185.
 38. Latt J, Brockstedt S, Wirestam R, Larsson E, Stahlberg F. Visualization of displacement-distribution parameters in q-space imaging. In: *Proc. 11th Annual Meeting ISMRM*, Toronto, Canada, 2003; 590.
 39. Chabert S, Meca CC, Le Bihan D. Relevance of the information about the diffusion distribution in vivo given by kurtosis in q-space imaging. In: *Proc. 12th Annual Meeting ISMRM*, Kyoto, Japan, 2004; 1238.